Materials Science & Engineering A 915 (2024) 147260

Contents lists available at ScienceDirect

Materials Science & Engineering A

journal homepage: www.elsevier.com/locate/msea

Creating heterostructures via laser powder bed fusion using titanium and stainless steel mixtures

Dingmeng Xu [a], Wuxin Yang [a,*], Malaya Prasad Behera [b], Sarat Singamneni [b], Michael A. Hodgson [a], Peng Cao [a,**]

[a] Department of Chemical and Materials Engineering, The University of Auckland, Private Bag 92019, Auckland 1142, New Zealand
[b] Department of Mechanical Engineering, Auckland University of Technology, New Zealand

ARTICLE INFO

Keywords:
Laser powder bed fusion
In-situ alloying
Heterostructures
Titanium
Stainless steel

ABSTRACT

This study addresses the challenge of breaking the trade-off dilemma between strength and ductility in additively manufactured Titanium (Ti) products. By leveraging concentration non-uniformity and controlled diffusion during in-situ alloying of unalloyed titanium (CP-Ti) and 316L stainless steel (SS316) powders via laser powder bed fusion (LPBF), we formulated a novel Fe-containing alloy with improved printability and enhanced mechanical performance. The microstructure of the as-built Ti alloy comprises a heterostructure of nano-scaled martensitic α′ within the micro-scaled equiaxed prior-β grains, resulting from rapid solidification inherent in LPBF. Since the modified laser-powder bed fusion in this work lacks a pre-heating function, a stress-relief annealing process was conducted to enhance the mechanical properties of the as-built parts. The annealed in-situ alloyed Ti-Fe achieves a superb balance between strength and ductility, with an ultimate tensile strength (UTS) of approximately 1118.0 MPa and an elongation of ~9.0 %. This study provides insights for designing high-performance Ti alloys with heterostructures using a mixture of elemental powder and alloyed powders via LPBF. The significance of concentration non-uniformity and diffusion during solidification is highlighted, demonstrating how these factors contribute to the formation of superior heterostructures through additive manufacturing.

1. Introduction

Titanium (Ti) and its alloys are renowned for their outstanding mechanical properties, high strength-to-weight ratio, excellent biocompatibility, and corrosion resistance, making them indispensable in aerospace, biomedical, automotive, and defense applications [1,2]. With escalating machining costs in conventional processes, metal-based additive manufacturing (AM) has emerged as a promising solution. Commonly known as 3D printing, AM revolutionizes manufacturing strategies by enabling the production of high-performance mechanical systems across various industries. A key advantage of metal-based AM lies in its near-net-shape forming capability, offering a wide range of technical benefits for processing complex geometries. These advantages include enhanced production rate, excellent design flexibility, and reduced material wastage. However, the full potential of AM for advancing the design and creation of new alloys has often been underestimated [3].

The unique thermal cycle and rapid cooling rate inherent in AM offer opportunities to develop heterogeneous alloys with location-specific compositions and microstructures to meet the specific requirements of engineering applications. These materials, referred to as compositional gradient or functionally graded materials (FGM), exhibit spatial gradients in their microstructure, leading to spatially varied mechanical properties. For instance, Wu et al. created a heterostructure in a Ti-55531 alloy through a three-step heat treatment process [4], resulting in a dual-phase microstructure with coarse and ultra-fine lamellar α precipitates. This heterostructured alloy demonstrated enhanced ductility due to the heterogeneous microstructure that prevents strain localization. It also exhibited high strength, attributed to the back stress effect induced by strain partitioning within the heterostructure. Similarly, Zhang et al. utilized LPBF to achieve partial homogenization of alloy melts (Ti-6Al-4V and stainless steel), producing heterostructures

* Corresponding author.
** Corresponding author.
E-mail addresses: wuxin.yang@auckland.ac.nz (W. Yang), p.cao@auckland.ac.nz (P. Cao).

https://doi.org/10.1016/j.msea.2024.147260
Received 10 June 2024; Received in revised form 29 August 2024; Accepted 9 September 2024
Available online 11 September 2024

with micrometre-scale concentration modulations. This resulted in a dual-phase microstructure of β and α′ martensite, exhibiting a transformation-induced plasticity (TRIP) effect that led to high tensile strength (~1.3 GPa) and excellent work-hardening capacity [5]. These examples illustrate the potential of AM techniques to create advanced materials with superior mechanical properties through microstructural engineering [6–8].

Additionally, the strategic design of hetero-phase boundaries can create Ti alloys with both high strength and good ductility. Zhang et al. developed a low-cost, strong, and ductile Ti-2.8Cr-4.5Zr-5.2Al alloy by leveraging the significant diffusion mismatch between Cr and Al to create high-density nano-martensitic interfaces [9]. The hierarchical structure of α'/β lamellae achieved a yield strength of 1266 MPa and an elongation of 12.6 %. Enhanced tensile properties are frequently observed in Ti alloys with micro- or nano-scaled α′ or α laths. These findings highlight the importance of designing multi-scale and multi-phase features to enhance mechanical properties.

One of the challenges in AM-fabricated Ti alloys is to mitigate the formation of coarse columnar grains, thereby reducing anisotropy and enhancing mechanical properties. Previous studies have explored various approaches, including the addition of alloying elements, manipulation of processing parameters, and post-processing heat treatments. Notably, modifying the constituents in Ti alloys to control the solidification mode of the high-temperature β phase has received significant attention. Iron (Fe) has been identified as an effective and economical β-stabilizer and grain refiner in Ti (where grain growth factor $Q_{Fe} \approx 3.8C_0$) [10]. It segregates ahead of the solidification interface, creating a local compositional supercooling zone that inhibits the mobility of the solid-liquid interface. For instance, Narayana et al. demonstrated that the addition of 4 wt% of Fe in directed energy deposition (DED) fabricated Ti-6Al-4V alloys successfully promoted the formation of near-equiaxed microstructure, achieving significant grain refinement [11]. However, increasing β stability by adding more Fe may suppress the Ti martensitic transformation and lead to the formation of isothermal ω, resulting in enhanced strength but reduced ductility. Similar findings were observed in LPBF-fabricated Ti-6Al-4V [12], Ti-5Fe [13], and DED-printed Ti-O-Fe alloys [14].

Recent advancements in the development of hierarchical microstructures have shown that the strategic design of multi-scale and multi-phase features can significantly improve mechanical properties [15,16]. The integration of heterogeneous microstructures through in-situ alloying of Ti with valuable β-stabilizing elements via advanced AM techniques like LPBF presents a promising approach to enhancing the mechanical properties of metal alloys. In this study, we aim to develop a novel Fe-containing Ti material through in-situ alloying of a mixed powder feedstock comprising commercially pure Ti (CP-Ti) and 316L stainless steel via LPBF. Leveraging the point-wise material consolidation unique capabilities typical of AM, the aim is to tailor the interior of the prior-β grains, resulting in a heterostructure induced by partial homogenization and limited diffusion during in-situ alloying. This approach holds the potential for simultaneously enhancing the strength and ductility of the final product. We hypothesize that through meticulous optimization of process parameters and appropriate post-processing heat treatment, the in-situ alloyed Fe-containing Ti alloy can achieve a favorable balance of strength and ductility. The in-situ alloying conditions, including materials mixture conditions and cooling rates, based on Flow 3D simulation results, are presented, providing valuable insights into developing Ti-based alloys through laser in-situ alloying by additively processing powder mixtures.

2. Experimental

2.1. Powder feedstock preparation

The raw powder feedstock consisted of commercially pure titanium (CP-Ti, Grade 1) and 316L stainless steel powders (SS 316L) supplied by ECKART TLS, with diameters ranging from approximately 10 to 45 μm. Table 1 displays the chemical compositions of CP-Ti and SS 316L. The mixed powder feedstock consisting of 94 wt% Ti and 6 wt% SS 316L was mixed in a rolling pot at 300 rpm for 24 h. Henceforth, this alloy is referred to as Ti-6SS.

Scanning electron microscopy (SEM) images in Fig. 1 depict the morphologies of the pre-alloyed powder SS 316L, elemental powder CP-Ti, and mixed powder feedstock Ti-6SS, respectively. The particle size distribution (PSD) of powder feedstock was measured by laser diffraction analysis (Malvern Mesmerizer 2000). The PSD of mixed powder feedstock was $D_{10} = 14.441\mu m$, $D_{50} = 30.358\ \mu m$, and $D_{90} = 53.265\mu m$.

2.2. LPBF process

The as-built Ti-6SS samples were fabricated using a Renishaw AM400 selective laser sintering system. This machine is equipped with an Nd: YAG laser operating at a wavelength of 1070 nm, with a maximum power output of 400 W and a laser spot size of 70 μm. All printing was done on Ti substrate plates. An argon atmosphere was maintained during processing to ensure oxygen content remained below 300 ppm.

The scanning strategy utilized was Meander, where the scanning direction rotates clockwise by 67° between adjacent layers. Optimization of process parameters for Ti-6SS was conducted through a trial-and-error approach, supplemented by computational modeling using Flow-3D to simulate the melting and solidification process (Section 2.5). The screening range for printing parameters was set at a power range of 300–360 W and a scan speed range of 1000–1400 mm/s. Based on microstructural observations, particularly in terms of porosity content, the scan speed and laser power were determined to be 1000 mm/s and 320 W. The layer thickness, hatch spacing, and substrate temperature were set at 40 μm60 μm and 200 °C, respectively.

2.3. Microstructural analysis

Phase identification of the Ti-6SS samples was conducted with X-ray diffraction (XRD) using Cu-Kα radiation, with a scan speed of 2°/min across a 2θ range of $20° - 80°$. To determine the induced porosity, optical microscopic (OM) images of the cross sections of printed samples were analyzed using ImageJ software, with three images analyzed per sample. Additionally, the Archimedes method was employed to measure the relative density of the as-printed Ti-6SS samples, with each sample measured three times [11]. The average density was found to be 4.63 g/cm^3, which closely matches the theoretical density of 4.64 g/cm^3.

The as-built samples intended for metallographic examination underwent a series of preparation steps. Initially, they were mechanically polished using 6 μm diamond suspension followed by finer polishing using colloidal silica up to 0.04 μm to achieve a smooth mirror surface. Subsequently, the samples were etched with Kroll's reagent (a solution consisting of 3 % HF, 5 % HNO_3, and 92 % H_2O by volume) for 20–30 s.

Metallographic and fractographic microstructures were characterized using a Hitachi SU-70 field emission scanning electron microscope (SEM) equipped with energy dispersive spectroscopy (EDS). Additionally, electron backscatter diffraction (EBSD) measurements were conducted utilizing an EBSD symmetry detector mounted on the ZEISS Cross Beam 550 FIB/SEM system, employing a step size of 0.03 μm. Standard mechanical grinding and electrochemical polishing procedures were employed to prepare specimens for EBSD measurements. The collected EBSD data was analyzed using AZtecCrystal software.

2.4. Mechanical evaluation

Nanoindentation tests were conducted on the printed Ti-6SS samples using the Hysitron TI-950 TriboIndenter. A three-sided pyramid Berkovich diamond indenter tip was used to evaluate the mechanical properties, including nano hardness (H) and reduced elastic modulus

Table 1
The chemical composition (wt%) of CP-Ti and SS 316L powder used in this work.

Composition (wt%)	Ti	Fe	O	C	N	H	Cr	Ni	Mo	Mn	Si	Cu	P	S
CP-Ti	Bal.	0.3	0.25	0.08	0.03	0.015	–	–	–	–	–	–	–	–
SS 316L	–	Bal.	0.02	0.024	0.09	–	17.6	12.5	2.29	0.77	0.63	0.02	0.007	0.005

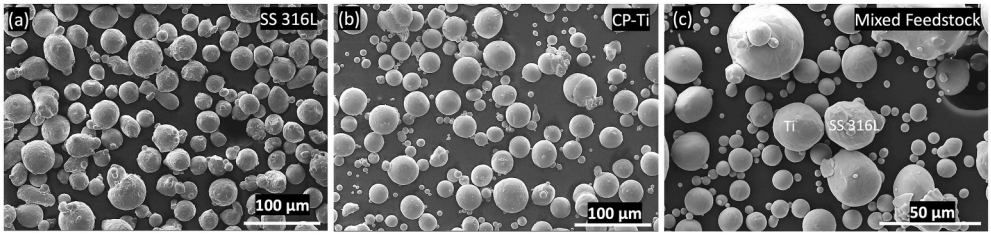

Fig. 1. SEM images of (a) SS 316L powder, (b) CP-Ti powder, and (c) Mixed powder feedstock of Ti-6SS.

(Er). The nanoindentation experiments were performed in selected areas measuring 40 µm × 40 µm. Each test run consisted of a series of 144 indents arranged in a 40 µm × 40 µm square pattern, with a spacing of 3 µm between indent locations. Following the nanoindentation tests, the indentation marks were examined using the Hitachi SU-70 scanning electron microscope (SEM).

Uniaxial tensile tests were conducted on dog-bone-shaped specimens with dimensions of 3 mm thickness, 14 mm width, 15 mm gauge length, and 39 mm total length, using a universal testing machine H50K-S Tinius Olsen equipped with a 10 mm extensometer. Three tensile samples were cut from different locations of the same LPBF-built coupon using electrical discharge machining (EDM). Prior to testing, the specimens underwent sanding down to a grit of 600 SiC paper to eliminate potential stress-raisers. The mechanical tests were performed at room temperature with a cross-head speed of 3 mm/min. Vickers microhardness of the Ti-6SS samples was measured using a load of 30 gf with a holding time of 15s. The average of 5 measurements was recorded as the hardness value.

The loading-unloading-reloading (LUR) test was conducted over seven cycles. For each cycle, the specimen was subjected to a pre-strain of 0.8 %. This cyclic loading sequence was applied to assess the material's mechanical response and to analyse its stress-strain behavior under repeated loading conditions.

2.5. Simulation

The discrete element method (DEM) in FLOW-3D (version 3.0.1.1.6 R7) was used to construct the powder bed, comprising a blend of CP-Ti and SS 316L powder. Subsequently, the FLOW-3D computational fluid dynamics (CFD) module (version 12.0 R7) was employed to simulate the melting and solidification process during 3D printing. This simulation facilitated the investigation of fluid dynamics and material mixture conditions throughout the in-situ alloying process, aiming to understand the printing process and its implications on the final microstructure of the printed samples.

3. Results

3.1. Microstructural characteristics

The XRD profile in Fig. 2 (a) illustrates that the dominant phase in the as-built Ti-6SS samples is β phases with body-cantered cubic (bcc) lattice structure. This β phase predominance is attributed to the retention of β in regions enriched with SS 316L elements (i.e., Fe, Cr, Ni, and Mo). The rapid cooling rate of LPBF, estimated at approximately 10^4–10^6 Ks^{-1} [17], induces martensitic transformation during cooling in regions with lower SS 316L element content, resulting in α' phase with a hexagonal close-packed (hcp) lattice: β→α'. Fig. 2 (b) and (c) present optical microscope (OM) and scanning electron microscope (SEM) images of the Ti-6SS samples, respectively, revealing a high density achieved with very few pores present. This observation confirms that the in-situ alloyed Ti-6SS, using mixed powder feedstock, exhibits a good density and high printability, consistent with the relative density of the samples.

In contrast to the typical coarse columnar grain morphology observed in most of the AM fabricated metals [12,13,17], the as-built Ti-6SS samples exhibit equiaxed grains with widths varying from approximately 10 to 50 µm along the building direction, as evident in

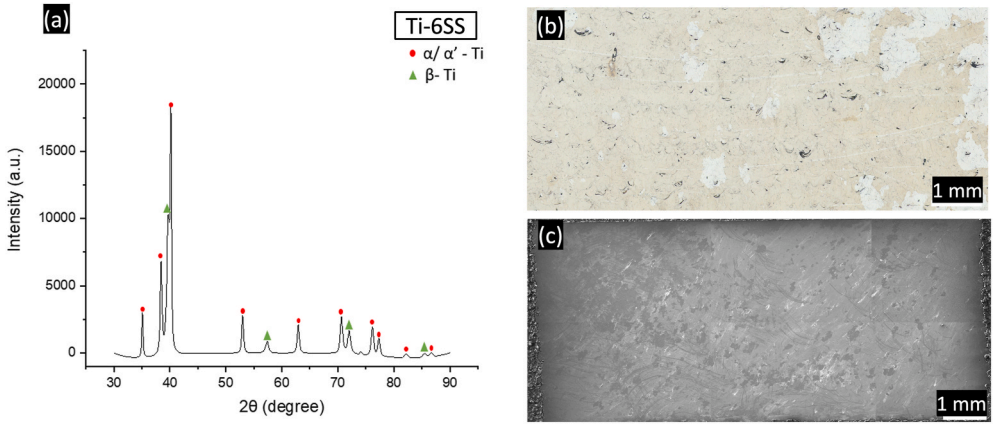

Fig. 2. (a) The XRD pattern of the Ti-6SS as-built sample. (b) Optical microscopic image of etched Ti-6SS printed sample. (c) SEM image of Ti-6SS printed sample.

Fig. 3 (a). Additionally, in Fig. 3 (b), smaller equiaxed grains are observed near the bottom of the melt pool boundary (MPB). This phenomenon can be attributed to the propensity of SS 316L powder, with higher density, to descend toward the melt pool boundary (MPB) and agglomerate, coupled with the insufficient diffusion of alloying elements over a short period. Consequently, a state of partial homogenization occurs, with β-stabilizing solute (viz., Fe, Cr, Ni, and Mo) segregation occurring at the lower extremity of the melt pool, where the influence of grain refinement is most pronounced. The SEM-EDS mapping in Fig. 3 (c) further confirms the segregation of Fe, Cr, and Ni at the bottom of the melt pool in the in-situ alloyed Ti-6SS sample.

The combined SEM image of the partial melt pool region in Fig. 4 (a) and the magnified specific site within the melt pool in Fig. 4 (b) reveals the presence of a needles-like structure within the prior β-grain. This needle-like structure is further confirmed to be α′ martensite through EBSD analysis, as depicted in Fig. 4 (c). The EBSD analysis shows a grouping of α′ needles parallel to each other, forming α′ martensitic clusters. The observation of such martensitic transformation, characterized by the needle-like morphology, is not surprising and is attributed to the rapid cooling rate during solidification. The band contrast image from EBSD in Fig. 4 (c) illustrates dark regions within the prior-β grains, indicating poor band contrast. This implies the undetectable, very fine martensitic structure, which is confirmed in the subsequent section.

The crystallography of the heterostructured α′ martensite formed within the prior-β grain after rapid cooling was extensively studied using EBSD. Fig. 5 (a) presents the inverse pole figure (IPF) map of the as-built Ti-6SS sample, showing equiaxed prior-β grains with varying sizes ranging from 10 to 50 μm. Upon close examination, the interior of some prior-β grains reveals the presence of α′ martensite, as observed in the enlarged IPF in Fig. 5 (b). The α′ martensitic plates are organized into groups of parallel variants, corresponding to the Burgers orientation relationship (BOR) $\{0001\}_{\alpha}//\{101\}_{\beta}$ and $<11\ \bar{2}\ 0>_{\alpha}//<1\ \overline{11}>_{\beta}$, characteristics of the diffusionless martensite transformation from the high-temperature BCC-β phase to the HCP α′ martensite [18]. This observation contrasts with the conventional formation pattern of martensite within the β grain matrix induced by rapid cooling, where martensitic α′ plates typically initiate at the β grain boundary and propagate in flaky-like or strip configurations entering the β grains. Notably, regions exhibiting slightly diminished contrast within the prior-β grains are believed to contain nano-sized martensite with thinner plates inFig. 5 (c). These regions are challenging to detect due to the limited resolution of the EBSD technique. Therefore, it implies the presence of not only martensitic α′ plates within the grain interior but also nano-sized martensite with thinner plates along the cooling rate gradient, traversing across prior-β grains from the center to the bottom of the melt pool.

3.2. Mechanical properties

3.2.1. Nanoindentation

Nanoindentation tests were conducted to investigate the nano-sized martensite within the prior-β grain of the as-built Ti-6SS material, highlighting the variations in nano-hardness and morphology at different regions away from the center of the melt pool. Three significant locations were identified within the testing region in Fig. 6 (a), denoted as areas b, d, and h, in the direction away from the center of the melt pool. The nano-hardness values measured in regions b and d are shown in Fig. 6 (b) and (d). Region 'b' exhibits lower nano-hardness values (4.16–5.88 GPa) compared to region 'd' (6.00–7.31 GPa), indicating softer martensitic structures in region 'b'. Fig. 6(c)–(e), and (h) present enlarged SEM images of the selected areas 'b', 'd', and 'h'. Fig. 6 (f) and (g) depict the variation of hardness and modulus of the Ti-6SS material,

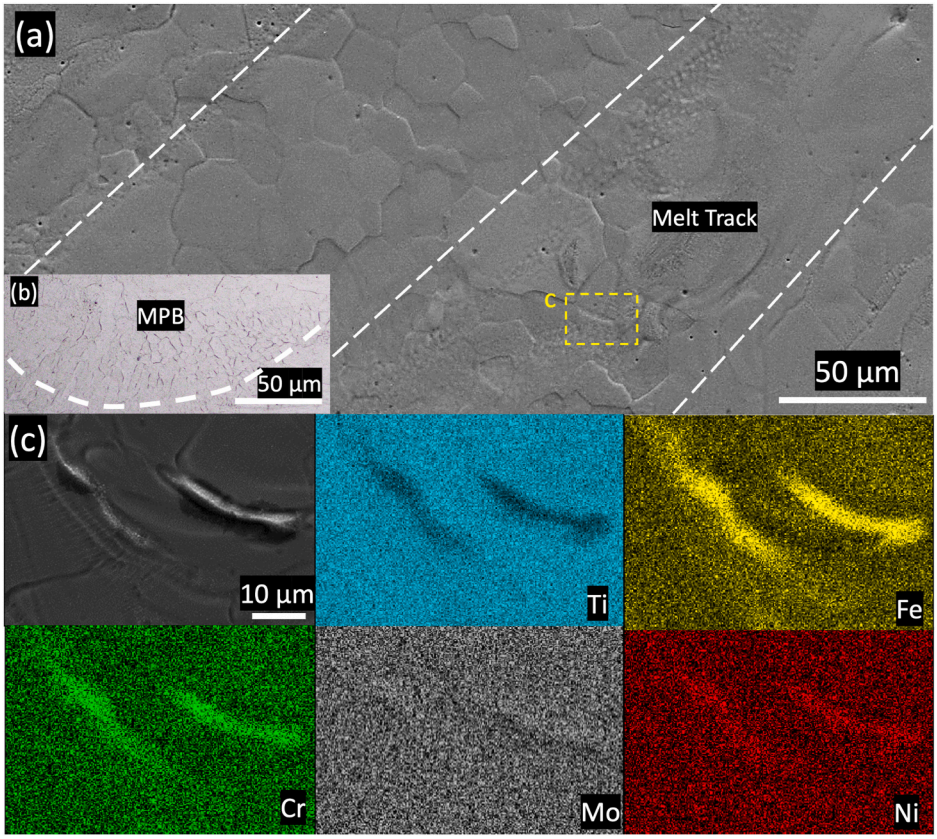

Fig. 3. (a) SEM image of Ti-6SS as-built sample showing equiaxed grains. (b) OM image of Ti-6SS as-built sample showing smaller equiaxed grains near the MPB. (c) SEM-EDS mapping showing the enrichment of SS 316L elements and depletion of Ti at the melt pool boundary. Note: EDS was conducted on the rectangular area in (a).

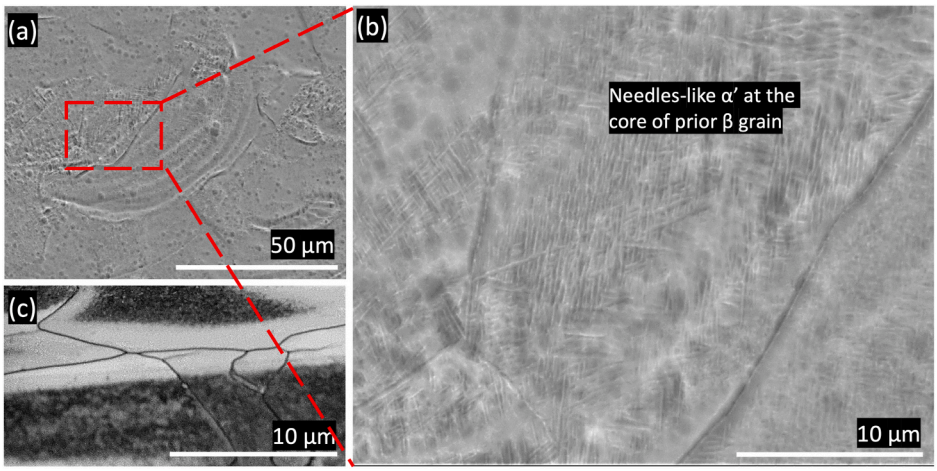

Fig. 4. (a) SEM image of melt pool region in the as-builtTi-6SS samples. (b) The enlarged image of the area is outlined in red. (c) EBSD band-contrast image of α′ martensite within the prior-β grain. (For interpretation of the references to colour in this figure legend, the reader is referred to the Web version of this article.)

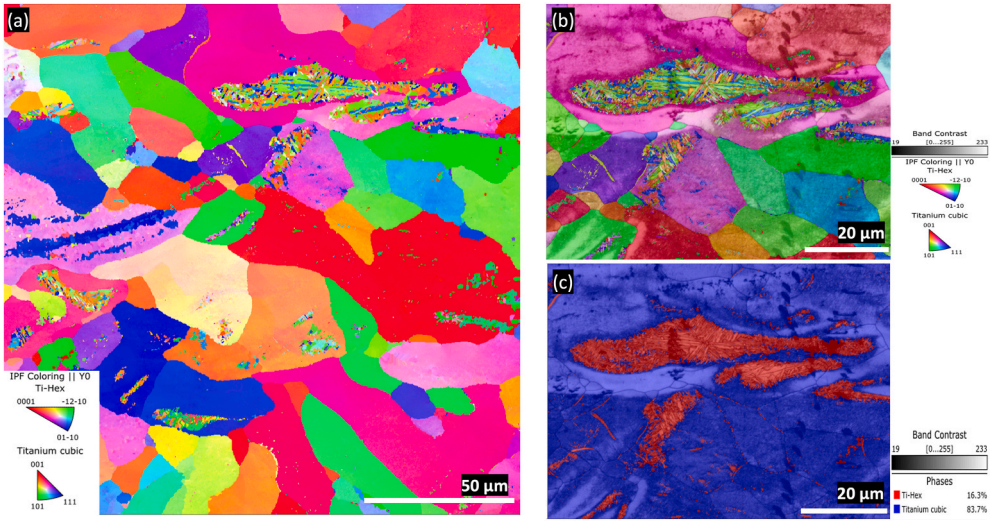

Fig. 5. (a) Inverse pole figure (IPF) map of the as-built Ti-6SS samples. (b) Enlarged IPF map of the selected area from (a). (c) Band contrast and phase map corresponding to (b).

wherein hardness and reduced modulus increase with the reduced width of the martensite plate. Notably, the α′ martensitic microstructure within the prior-β grain reveals different morphologies with a reduction in the lath of martensite: transitioning from relatively coarser parallel lath-shaped α′ with an approximate width of 110 nm to refined zigzag-structured α′ (~80 nm), culminating in further refinement to acicular-shaped α′ in multi-orientations (<50 nm). The observed refinement of martensitic laths increases the density of interfaces, which act as barriers to dislocation motion during deformation, thus enhancing the material's hardness. The mechanism of heterostructured martensite formation with thin laths will be discussed in Section 4.

The as-built Ti-6SS material displays a heterogeneous structure of nano-sized martensite within the prior β grains, exhibiting various morphologies from ordered short laths to refined acicular shapes. This diverse structure is anticipated to provide a favorable balance between strength and ductility by combining both soft and hard phases. However, the absence of the pre-heating function in the modified LPBF machine induced significant residual stress in the as-built microstructure. To address this issue, we performed tress-relief annealing at 565 °C for 1 h, followed by air cooling. The annealing temperature and duration were chosen to reduce residual stresses while preventing martensite α' from complete decomposition into stable α and β phases.

3.2.2. *Tensile testing and fractography*

Fig. 7 displays the stress-strain curves obtained for LPBF-printed Ti-6SS specimens under different conditions (as-built and stress-relieved). As-built samples exhibit rupture in the elastic stage and achieve a strength of approximately 996 MPa while demonstrating no visible ductility. In contrast, the stress-relieved Ti-6SS samples (represented by the green, red, and blue curves) exhibit a substantial improvement in ductility, with elongation to failure achieving approximately 9.0 %. Slight variations in the tensile curves among the stress-relieved samples were observed, likely due to subtle differences in microstructures. Nevertheless, all stress-relieved samples exhibit superior ductility and adequate tensile strength, making them more suitable for practical applications compared to their as-built counterparts. The mechanical properties of Ti-6SS under various conditions are summarized in Table 2, which correlates with the fracture features observed in Fig. 8.

As shown in Fig. 8, the as-built sample displays a typical river-like brittle material pattern with prominent flat facets, while the annealed Ti-6SS exhibits larger, deeper dimples, indicative of improved ductility. Notably, the size of facets in the as-built Ti-6SS sample is comparable to the size of prior-β grains, suggesting intergranular fracture.

Table 3 summarizes the mechanical properties of various Ti alloys processed by different manufacturing methods. The comparison reveals

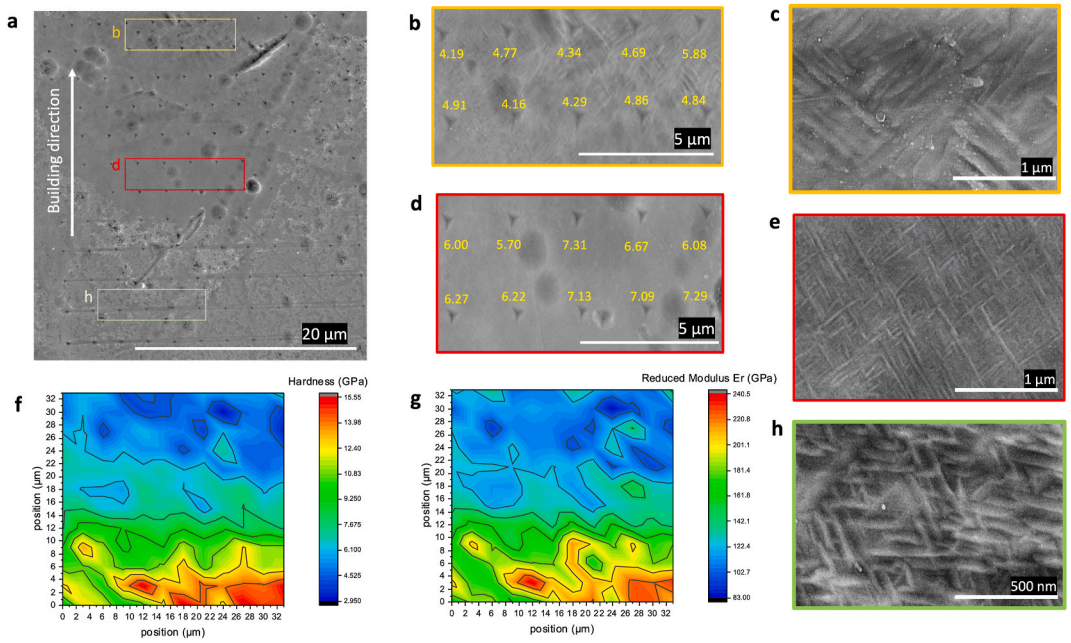

Fig. 6. (a) SEM image of the selected testing area. (b) The enlarged image of marked area b from (a) with nano-hardness value. (c) The enlarged image of (b). (d) The enlarged image of marked area d from (a) with nano-hardness value. (e) The enlarged image of (d). (h) The enlarged image of marked area h in (a). (f) and (g) are the hardness and modulus mapping of the Ti-6SS sample, respectively.

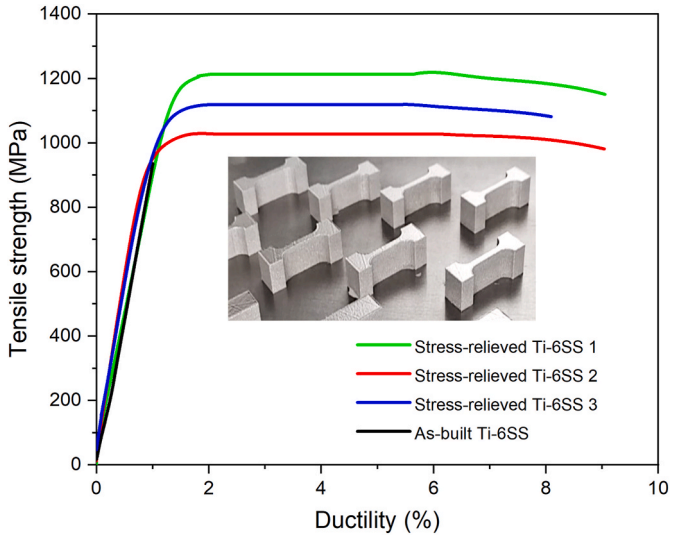

Fig. 7. Stress-strain curves of Ti-6SS at the as-built state and after stress relief.

Table 2
Mechanical properties of Ti-6SS samples under various conditions.

Condition	UTS (MPa)	ε (%)	Micro-hardness (VHN)
As-built	996.0 ± 69.0	0.4 ± 0.13	518.2
Stress-relieved at 565 °C	1118.0 ± 79.0	9.0 ± 0.53	347.3

that the in-situ alloying of CP-Ti and SS 316L powder via LPBF is a viable approach to fabricating Fe-containing Ti alloy with enhanced mechanical properties. The resulting material exhibits superior strength and ductility compared to as-sintered Ti-5Fe [19]. Its strength is comparable to that of LPBF fabricated Ti-6Al-4V with heat treatment but with a slightly diminished ductility [20]. These findings highlight the effectiveness of multiple β-stabilizing elements (i.e., Fe, Cr, Ni, Mo) from SS 316L powder to strengthen Ti. Moreover, the blended CP-Ti and SS 316L powder show promise in potentially replacing expensive gas-atomized pre-alloyed Ti-6Al-4V powder under certain conditions. Furthermore, stress-relief post-processing is effective in enhancing the mechanical performance of in-situ alloyed Ti alloys.

3.3. Microstructural observations of annealed Ti-6SS

Fig. 9 shows the SEM images of the heat-treated Ti-6SS material. In Fig. 9 (a), the heat-treated microstructure exhibits a heterogeneous arrangement of martensite α′ within the prior β grain. The martensite α′ appears well-defined and more organized compared to the as-built state, indicating the stabilization and coarsening processes that occurred during heat treatment. Fig. 9 (b) provides a closer view of the microstructure within the highlighted region in Fig. 9 (a). The martensite α' exhibits varying lath sizes, with Fig. 9 (b1) displaying a coarser and more organized structure, indicating an inhomogeneous distribution of alloying elements. The EDS line scan across the heterogeneous region in Fig. 9 (c) shows increased Fe content along the scanned line from region b1 to region b2. The stress-relief annealing leads to a distribution of fine and coarse martensitic structures akin to those observed in Ti-55531 alloy [4], where heterostructures remain stable because the high-density interfaces and alloying elements stabilize these phases.

4. Discussion

Extensive efforts have been dedicated to achieving homogenization in in-situ alloying via PBF, with investigations spanning various strategies such as remelting, modifying powder feedstock, and adjusting processing parameters. However, in this study, we focus on leveraging the partial homogenization of elemental melts to enhance the in-situ alloyed microstructure of Ti-6SS with suitable post-heat treatment, thereby improving its mechanical properties.

4.1. Formation mechanisms of heterostructures

The formation of heterostructures in Ti-6SS alloys via LPBF results in nano-scaled martensitic α′ within micro-scaled equiaxed prior-β grains.

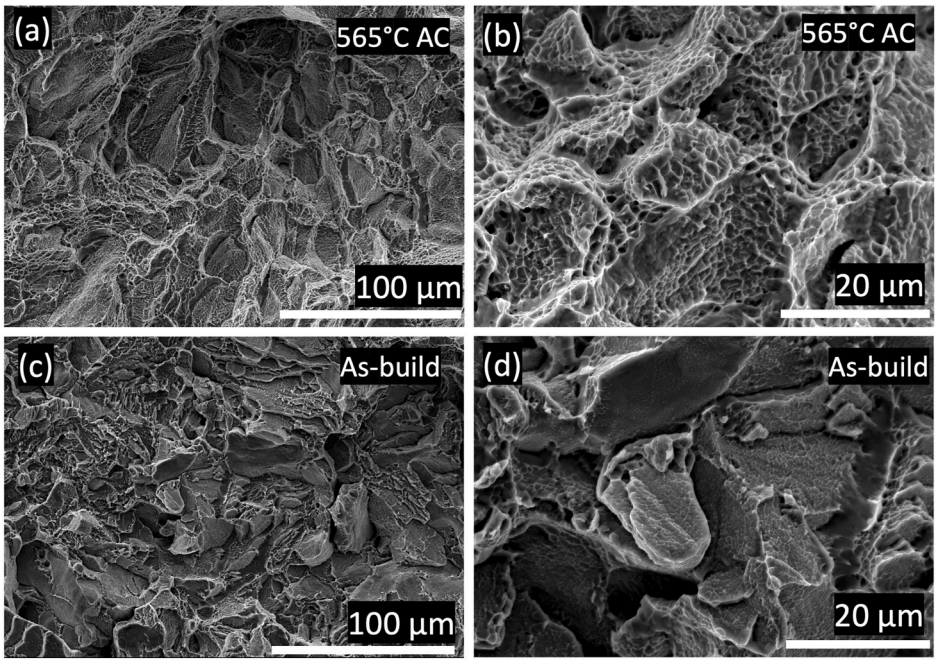

Fig. 8. SEM fractography of (a) as-built Ti-6SS, (b) the corresponding enlarged image of (a), (c) annealed at 565 °*C* AC condition, (d) the corresponding enlarged image of (d).

Table 3
Comparison of the mechanical properties of CP-Ti processed by different manufacturing methods.

Material	UTS (MPa)	Ductility (ε) (%)	Ref
As-cast Ti-3Fe	667.0	15.5	[21]
LPBF in-situ alloyed Ti-5Fe (stress relief)	945.0	4.5	[13]
LPBF in-situ alloyed Ti-5Fe-0.2Y & heat-treated	865.0	12.2	[13]
As-sintered Ti-5Fe	930.0	2.7	[19]
SLM Ti-6Al-4V + 3 wt% Fe heat-treated	1112.0	13.6	[20]
LPBF Ti-6AL-4V + 4.5 % SS316	1300.0	99.0	[5]
LPBF in-situ alloyed Ti-6SS (stress relief)	1118.0	9.0	This work

This process is driven by the rapid solidification of AM and the resulting chemical homogeneity and concentration gradient of alloying elements. Fig. 10 illustrates the microstructural evolution of Ti-6SS in the as-built state. This schematic depiction is based on our microstructural observations. The sequence of microstructural features progresses from fine parallel lath-shaped α′ to refined zigzag-structured α′, and super-refined acicular-shaped α', moving from the center to the bottom of the melt pool (Fig. 10). This progression resembles previous studies on the microstructure development of LPBF-fabricated CP-Ti parts [22,23].

4.1.1. *Concentration gradient of β-stabilizing elements*

The rapid cooling during the LPBF process strongly limits the diffusion length of alloying elements, resulting in a concentration gradient of β-stabilizing elements (e.g., Fe, Cr, Ni, Mo), which promotes heterogeneous nucleation and growth of martensite. This non-uniform distribution enhances the alloy's strengthening capacity by inducing local strains that impede dislocation motion. Regions enriched with SS 316L elements (e.g., Fe, Ni, Cr, Mo) remain as softer β-phase shells, while SS 316L poor regions form harder α′ martensite cores. The hard α′ martensite core consists of nano-scaled α′ martensite with varied morphology due to the concentration gradient of alloying elements, primarily Fe. Fig. 11 shows the EDS line scan revealing an increasing Fe content with decreasing martensite lath size, resulting in a gradient that drives the formation of microstructural heterogeneity. Similar to findings in TiAl alloys, the interplay between the number density of nuclei and coalescence events during growth leads to a refined microstructure with varying martensitic morphologies [24]. Furthermore, this is also parallel to earlier studies of creating nano-martensitic Ti alloys with the finest size [9].

The partial homogenization of local melts is further substantiated through Flow-3D simulation (Fig. 12), which demonstrates the non-uniform spreading of SS 316L over Ti during melting. The kinetic energy in the melt pool during in-situ alloying primarily arises from the Marangoni forces and thermal flux. However, due to the comparable particle size of Ti and SS 316L powders and relatively low SS 316L content in the powder mixture feedstock, coupled with rapid cooling in the LPBF process, SS 316L fails to uniformly disperse across a large area in the melt pool within the limited timeframe, leading to approximately 33 % localized enrichment of SS 316L content.

As shown in Fig. 13, the multi-track simulation offers insights into the in-situ alloying process during PBF, revealing the non-uniform distribution of Ti and SS 316L powders, which leads to local enrichment of SS 316L elements and the formation of a heterostructured martensite. This numerical evidence supports the observed heterostructured martensite within the as-built Ti-6SS alloy.

4.1.2. *Cooling rate variations*

The thermo-physical properties of the alloying elements and melt-pool dynamics during LPBF contribute to the formation of heterostructures. The differences in thermal conductivity and melting points between Ti and SS 316L affect the melt-pool behavior, leading to localized variations in cooling rates, which further promote heterogeneity. The gradient in cooling rate across the laser track and multiple melt pools, from the top to the bottom, results in martensitic laths with various morphologies: coarser parallel martensitic plates, refined zigzag-structured martensitic α′ plates, and super-refined acicular-shaped martensitic α′ plates. The $\alpha \rightarrow \beta \rightarrow \alpha'/\alpha$ transition in Ti is governed by the Burgers orientation relationship (BOR), which predicts 12 possible α variants in one prior-β grain [25]. However, deviations from the expected theoretical texture, known as variant selection, are observed,

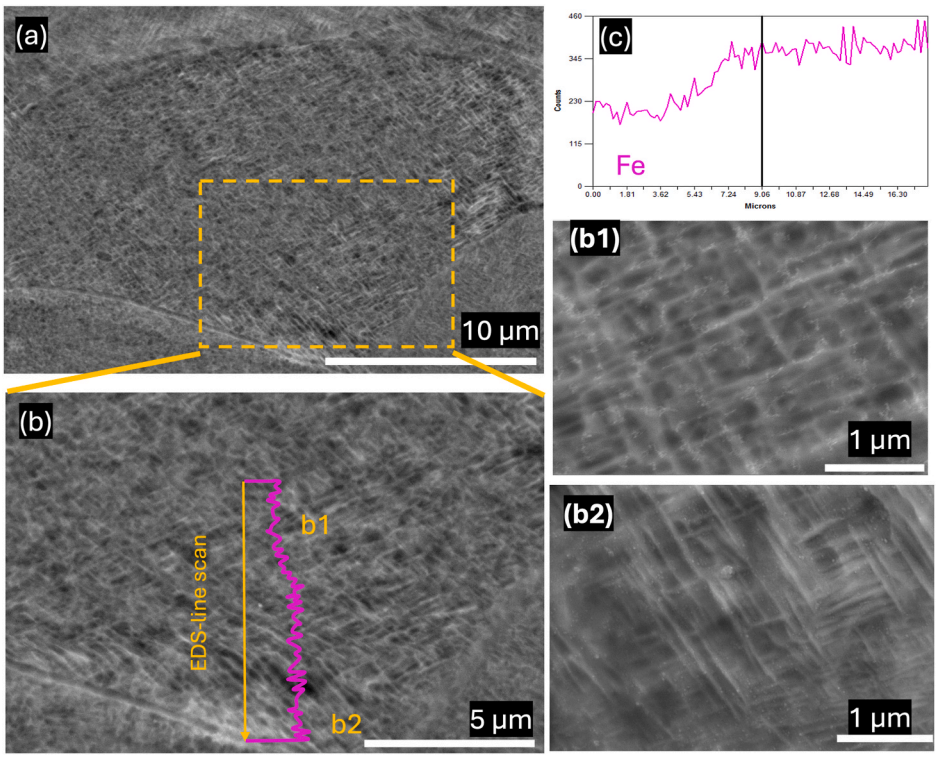

Fig. 9. (a) Overview of the annealed microstructure showing a heterogeneous arrangement of martensite α'. (b) Closer view of the highlighted region in (a). (c) EDS line scan across the heterogeneous region. (b1) Region with coarser and more organized martensite α′ structure. (b2) Region with finer martensite α′ structure.

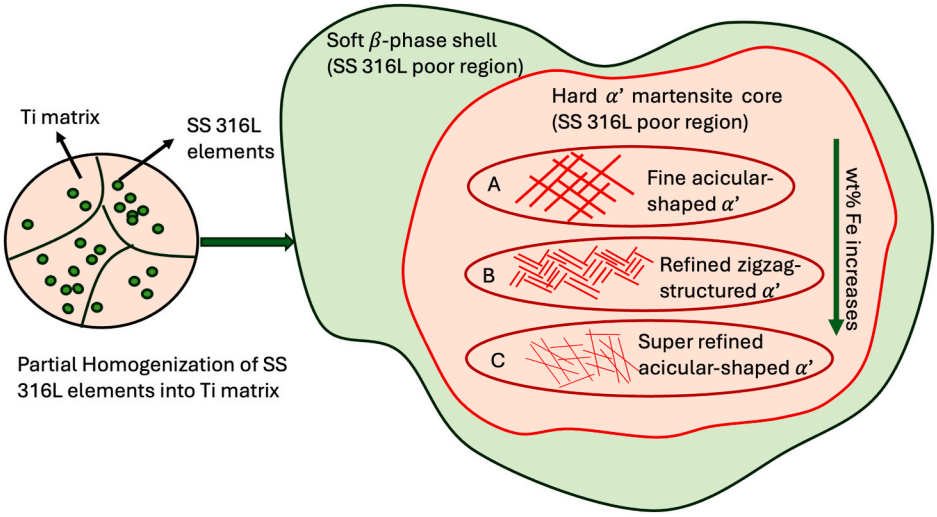

Fig. 10. Schematic illustration of microstructural evolution of as-printed Ti-6SS.

particularly in AM-fabricated Ti alloys. In this study, variant clusters are observed to minimize transformation strain for the intragranular formation of α/α' within the prior-β grain in the as-built Ti-6SS sample. This self-accommodation of martensitic lath for variant selection has been documented in previous studies [26]. Several parameters affect the variant selection mechanism during the martensite phase transition in Ti, mainly related to the prior-β grain characteristics such as grain size, orientation, residual stress, and thermal properties, including cooling rate [27]. This observation aligns well with the previous work by Yao et al., where adjusting hatch spacing to achieve a higher cooling rate induced weak variant selection during the martensite phase transition [28].

The gradient in cooling rate across laser track and multiple melt pools, from the top to the bottom, results in martensitic laths with various morphologies: relatively coarser parallel martensitic plates, refined martensitic α′ plates in organized zigzag form, and super-refined acicular-shaped martensitic α' plates. At the outermost center of the melt pool with the highest cooling rate, faster kinetics produce variants with equal probability, resulting in a finer needles-like martensite structure with a random texture. As the cooling rate decreases towards the center of the melt pool, the likelihood of producing martensite structures with more textured microstructure and a higher degree of variant selection increases.

The changes in cooling rates during in-situ alloying of dissimilar SS 316L and CP-Ti powders are further confirmed by Flow-3D fluid dynamic simulations. This study involves multiple materials of Ti and SS

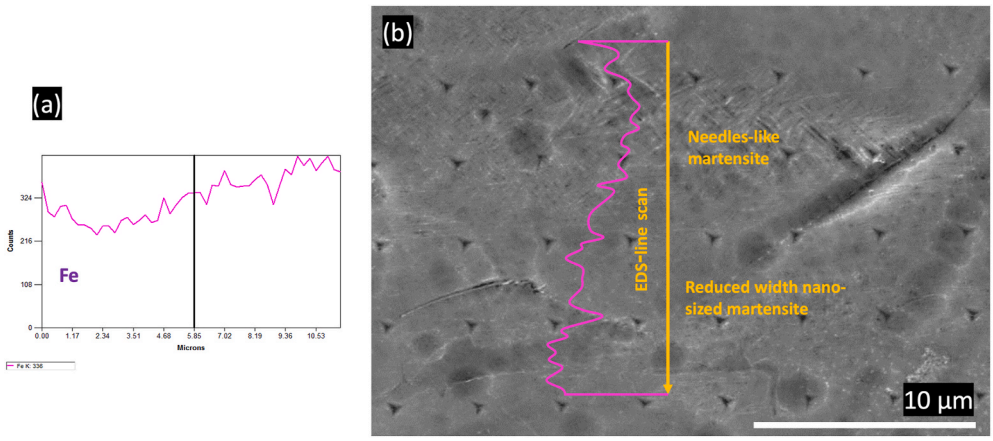

Fig. 11. EDS line scan across the specific heterostructure site.

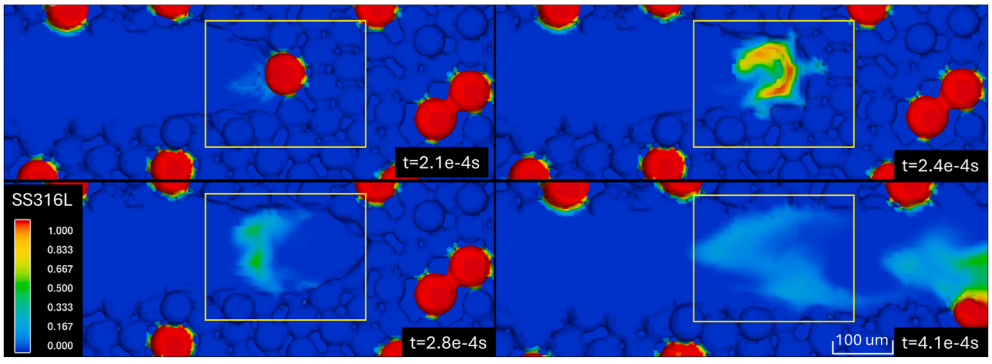

Fig. 12. Fluid dynamic simulations revealing the in-situ alloying condition for a single particle. The blue particle indicates the CP-Ti powder, and the red particles are the SS 316L powder. (For interpretation of the references to colour in this figure legend, the reader is referred to the Web version of this article.)

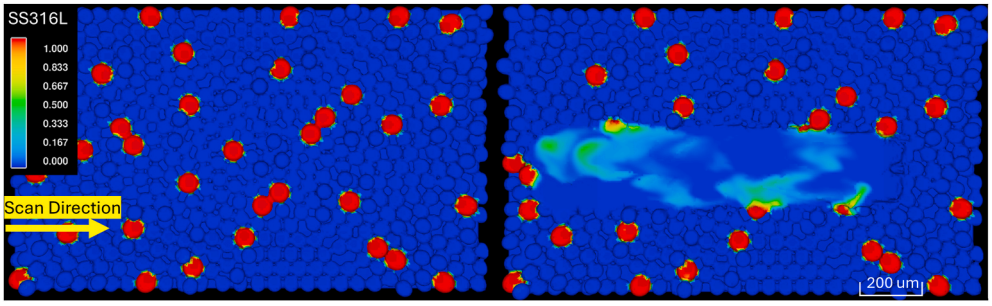

Fig. 13. Multi-track simulations for revealing the in-situ alloying condition. The blue particle indicates the CP-Ti powder, and the red particles are the SS 316L powder. (For interpretation of the references to colour in this figure legend, the reader is referred to the Web version of this article.)

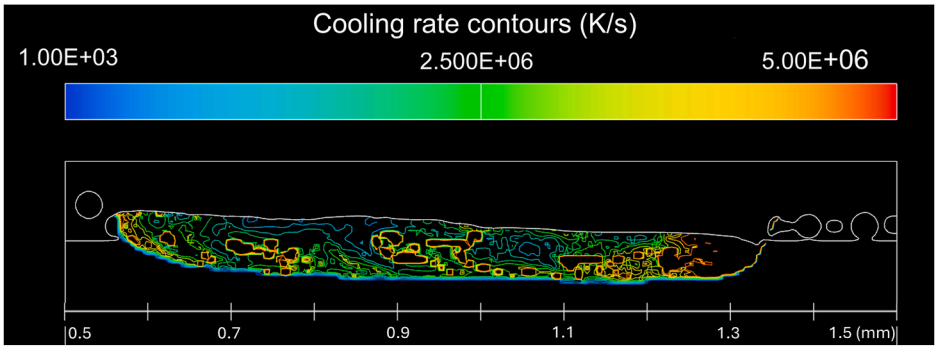

Fig. 14. The fluid dynamic simulation for cooling rate contour values in single laser track during in-situ alloying.

316L and takes into account the presence of Ar gas. Hence, the transient nature of the LPBF process, along with interactions among the laser beam, powder bed, surrounding environment, and diverse materials, induces dynamic alterations in temperature gradients and cooling rates within the melt pool. Fig. 14 shows that the cooling rate exhibits a wide range varying from the magnitude of 10^3 to 10^6 within the powder bed. The changes in cooling rates significantly impact the kinetics, leading to the formation of heterostructured martensite.

4.2. Role of heterostructures in enhancing mechanical properties

Due to significant residual stress, the ductility did not meet expectations in the as-built state. Therefore, low-temperature annealing was conducted primarily to reduce residual stress, albeit at the expense of homogenization and coarsening. However, the heterogeneity remains intact, and the synergistic effects are retained post-annealing, as demonstrated by improved ductility.

In the heat-treated Ti-6SS material, a heterogeneous distribution of α and retained β phases accommodates plastic deformation. Under tensile loading, the soft retained β phases (rich β-stabilizing elements region) and α phase (lean β-stabilizing elements area) will be plastically deformed first. The well-defined, coarser martensite α' plates provide high strength due to their relatively stable and coherent structure. The presence of nano-sized martensitic structures (i.e., substructural complexities) further prevents strain localization, acting as effective barriers against dislocation motion, increasing the strength even more through dislocation pinning. The plastic incompatibility from micro to nano-scale of soft and hard phases presents at hetero-interfaces where the dislocations are produced to help with compatible deformation during deformation. These geometrically necessary dislocations (GNDs) induce heterogenous deformation-induced (HDI) strengthening [29,30].

The HDI strengthening is a key mechanism driving the synergistic enhancement of mechanical properties in Ti-6SS. This is evidenced by the results from the loading-unloading-reloading (LUR) test shown in Fig. 15 (a). Each unload-reload cycle exhibits an increasement in stress with strain with the persistent hysteresis loops, indicating that HDI stress (σ_{HDI}) is active during tensile deformation [31]. To quantify the HDI effect, HDI stress is calculated from the following equations:

$$\sigma_{HDI} = \sigma_{flow} - \sigma_{eff} \text{ and } \sigma_{eff} = \frac{\sigma_{flow} - \sigma_u}{2} + \frac{\sigma^*}{2} \quad [32]$$

The HDI stress-strain relationship, plotted in Fig. 15 (b), reveals a progressive increase in HDI stress with strain. This trend highlights the role of the heterostructure in obstructing dislocation motion, necessitating higher internal stresses to continue plastic deformation.

EBSD analysis was further used to elucidate how the heterostructure in the Ti-6SS material contributes to its mechanical properties through HDI strengthening. Fig. 16 (a) and (b) present the Inverse Pole Figure (IPF) and Kernel Average Misorientation (KAM) maps of the Ti-6SS material before deformation. These maps indicate low misorientation levels and minimal internal strain within the heterostructure, which comprises multiple phases with distinct orientations. Upon 8 % deformation, as shown in Fig. 16(c) and (d), the IPF and KAM maps reveal significant changes. The deformation induces increased misorientation within the grains, accompanied with a higher density of low-angle grain boundaries, suggesting active dislocation movement and rearrangement. Notably, the sharp rise in KAM values at the phase interfaces indicates that these boundaries act as robust barriers to dislocation motion, thereby contributing to HDI strengthening. The accumulation of dislocations at these interfaces generates HDI stress (also known as back stress), which impedes further dislocation movement in adjacent grains, enhancing the material's resistance to additional deformation.

5. Conclusions

In this study, we successfully fabricated a Fe-containing Ti alloy (Ti-6SS) with high printability through in-situ alloying of mixed powder feedstock of commercially pure titanium and stainless steel 316L powders by LPBF. By leveraging concentration non-uniformity caused by partial homogenization of two dissimilar metal melts, a heterostructure in the as-built state was achieved. Heterogeneity remains intact after a mild stress relief annealing treatment. Key findings from our investigation are summarized below.

- Microstructural analysis reveals micro-scaled equiaxed prior-β grains comprising nano-scaled martensitic α′ with varying laths and structures. This transition manifests from relatively coarser parallel lath-shaped α' (~110 nm) to refined zigzag structured α' (~80 nm) and further progressing to acicular-shaped α′ displaying multi-orientations (<50 nm). This evolution occurs from the center region toward the bottom of the melt pool.
- The UTS and ductility of the LPBF-fabricated Ti-6SS alloy reach 1118.0 MPa and 9.0 %, respectively, implying a favorable balance between strength and ductility akin to typical AM-fabricated Ti-based alloys.
- The formation of heterostructured martensite within the as-built microstructure is enabled by actively utilizing concentration non-uniformity resulting from partial homogenization, influenced by variations in cooling rate and the compositional differences of β-stabilizing elements (Fe, Cr, Ni, Mo).
- Annealing at low temperatures enhances mechanical properties by reducing residual stresses effectively. It preserves the heterogeneity, characterized by well-defined martensite α′ plates and some equiaxed and elongated α grains with retained β phase.

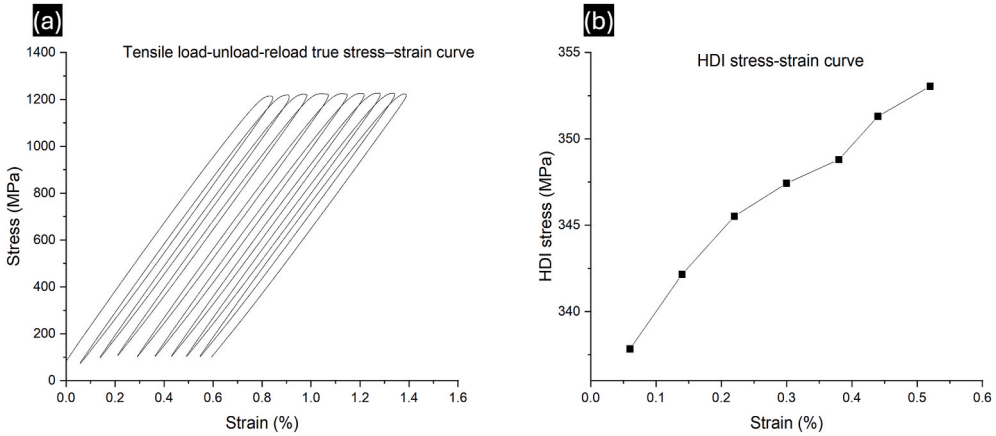

Fig. 15. (a) Tensile load-unload-reload (LUR) true stress-strain curve in Ti-6SS. (b) Plot of HDI stress with applied strain.

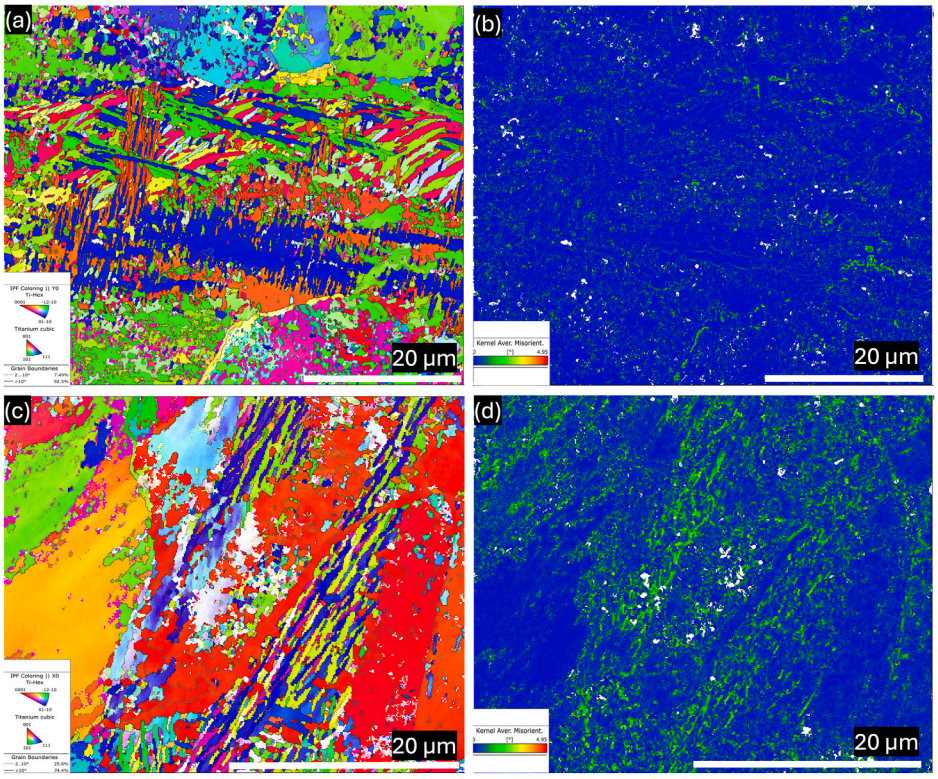

Fig. 16. (a) Inverse Pole Figure (IPF) of Ti-6SS material before deformation. (b) Kernel Average Misorientation (KAM) map of Ti-6SS material before deformation. (c) IPF map of Ti-6SS material after 8 % deformation. (d) Ti-6SS material after 8 % deformation.

- The Ti-6SS material exhibits enhanced mechanical properties primarily due to HDI strengthening, where the heterostructure, comprising distinct phases and orientations, impedes dislocation motion, leading to increased back stress, and effective dislocation pile-up at phase interfaces.

Our study offers guidance for designing high-performance novel alloys with heterostructure through in-situ alloying of mixed feedstock of elemental powder and pre-alloyed powder containing multiple alloying elements by LPBF. Future research should investigate various heat treatments to further enhance the mechanical properties of Ti-6SS and to understand the role of the heterostructure in the heat-treated states.

CRediT authorship contribution statement

Dingmeng Xu: Writing – original draft, Methodology, Investigation, Formal analysis. **Wuxin Yang:** Writing – review & editing, Investigation, Formal analysis. **Malaya Prasad Behera:** Investigation. **Sarat Singamneni:** Writing – review & editing, Methodology. **Michael A. Hodgson:** Writing – review & editing, Formal analysis. **Peng Cao:** Writing – review & editing, Supervision, Funding acquisition, Conceptualization.

Declaration of competing interest

The authors declare that they have no known competing financial interests or personal relationships that could have appeared to influence the work reported in this paper.

Data availability

Data will be made available on request.

Acknowledgments

This work was funded by the Royal SocietyTe Apārangi through its Marsden Fund (Grant no. UOA2114).

References

[1] C. Leyens, M. Peters, Titanium and Titanium Alloys: Fundamentals and Applications, Wiley Online Library2006.
[2] P. Cao, L. Zhang, Titanium alloys: basics and applications, World Scientific (2024).
[3] W.E. Frazier, Metal additive manufacturing: a review, J. Mater. Eng. Perform. 23 (6) (2014) 1917–1928.
[4] D. Wu, M. Hao, T. Zhang, Z. Wang, J. Wang, G. Rao, L. Zhang, C. Ding, K. Zhou, L. Liu, D. Wang, Y. Wang, Heterostructures enhance simultaneously strength and ductility of a commercial titanium alloy, Acta Mater. 257 (2023) 119182.
[5] T. Zhang, Z. Huang, T. Yang, H. Kong, J. Luan, A. Wang, D. Wang, W. Kuo, Y. Wang, C.-T. Liu, In situ design of advanced titanium alloy with concentration modulations by additive manufacturing, Science 374 (6566) (2021) 478–482.
[6] Y.P. Dong, J.C. Tang, D.W. Wang, N. Wang, Z.D. He, J. Li, D.P. Zhao, M. Yan, Additive manufacturing of pure Ti with superior mechanical performance, low cost, and biocompatibility for potential replacement of Ti-6Al-4V, Mater. Des. 196 (2020) 109142.
[7] D.W. Wang, Y.H. Zhou, J. Shen, Y. Liu, D.F. Li, Q. Zhou, G. Sha, P. Xu, T. Ebel, M. Yan, Selective laser melting under the reactive atmosphere: a convenient and efficient approach to fabricate ultrahigh strength commercially pure titanium without sacrificing ductility, Mater. Sci. Eng. 762 (2019) 138078.
[8] H.Z. Niu, S. Liu, M.C. Zang, D.L. Zhang, P. Cao, W.X. Yang, Anomalous strain rate dependence of ultra-low temperature strength and ductility of an electron beam additively manufactured near alpha titanium alloy, J. Mater. Sci. Technol. 198 (2024) 44–55.
[9] C. Zhang, X. Bao, M. Hao, W. Chen, D. Zhang, D. Wang, J. Zhang, G. Liu, J. Sun, Hierarchical nano-martensite-engineered a low-cost ultra-strong and ductile titanium alloy, Nat. Commun. 13 (1) (2022) 5966.
[10] M.J. Bermingham, S.D. McDonald, D.H. StJohn, M.S. Dargusch, Beryllium as a grain refiner in titanium alloys, J. Alloys Compd. 481 (1) (2009) L20–L23.
[11] P.L. Narayana, S. Lee, S.-W. Choi, C.-L. Li, C.H. Park, J.-T. Yeom, N.S. Reddy, J.-K. Hong, Microstructural response of β-stabilized Ti–6Al–4V manufactured by direct energy deposition, J. Alloys Compd. 811 (2019) 152021.
[12] M. Simonelli, D.G. McCartney, P. Barriobero-Vila, N.T. Aboulkhair, Y.Y. Tse, A. Clare, R. Hague, The influence of iron in minimizing the microstructural anisotropy of Ti-6Al-4V produced by laser powder-bed fusion, Metall. Mater. Trans. 51 (5) (2020) 2444–2459.

[13] H. Wang, H.L. Luo, J.Q. Chen, J.C. Tang, X.Y. Yao, Y.H. Zhou, M. Yan, Cost-affordable, biomedical Ti-5Fe alloy developed using elemental powders and laser in-situ alloying additive manufacturing, Mater. Char. 182 (2021) 111526.
[14] T. Song, Z. Chen, X. Cui, S. Lu, H. Chen, H. Wang, T. Dong, B. Qin, K.C. Chan, M. Brandt, X. Liao, S.P. Ringer, M. Qian, Strong and ductile titanium–oxygen–iron alloys by additive manufacturing, Nature 618 (7963) (2023) 63–68.
[15] K.-H. Jin, C. Liu, J. Ye, W. Yang, Y. Fang, X. Wei, J. Jin, Q. Ding, H. Bei, X. Zhao, Z. Zhang, Achieving enhanced tensile strength-ductility synergy through phase modulation in additively manufactured titanium alloys, Mater. Sci. Eng. 909 (2024) 146801.
[16] H. Schaal, P. Castany, T. Gloriant, Outstanding strain-hardening of a new metastable β-titanium alloy elaborated by in situ additive manufacturing L-PBF process, Mater. Sci. Eng. 875 (2023) 145117.
[17] E.A. Lass, M.R. Stoudt, M.E. Williams, M.B. Katz, L.E. Levine, T.Q. Phan, T. H. Gnaeupel-Herold, D.S. Ng, Formation of the Ni3Nb δ-phase in stress-relieved inconel 625 produced via laser powder-bed fusion additive manufacturing, Metall. Mater. Trans. 48 (11) (2017) 5547–5558.
[18] V. Tong, S. Joseph, A.K. Ackerman, D. Dye, T.B. Britton, Using transmission Kikuchi diffraction to characterise α variants in an α+β titanium alloy, J. Microsc. 267 (3) (2017) 318–329.
[19] Y. Alshammari, S. Raynova, F. Yang, L. Bolzoni, Effect of particle size and manufacturing technique on the properties of the PM Ti-5Fe alloy, Int. J. Refract. Metals Hard Mater. 90 (2020) 105246.
[20] M. Simonelli, Z. Zou, P. Barriobero-Vila, Y.Y. Tse, The development of ultrafine grain structure in an additively manufactured titanium alloy via high-temperature microscopy, Materialia 30 (2023) 101856.
[21] J. Niu, Y. Guo, K. Li, W. Liu, Z. Dan, Z. Sun, H. Chang, L. Zhou, Improved mechanical, bio-corrosion properties and in vitro cell responses of Ti-Fe alloys as candidate dental implants, Mater. Sci. Eng. C 122 (2021) 111917.
[22] D. Zhang, D. Qiu, M.A. Gibson, Y. Zheng, H.L. Fraser, D.H. StJohn, M.A. Easton, Additive manufacturing of ultrafine-grained high-strength titanium alloys, Nature 576 (7785) (2019) 91–95.
[23] M.J. Bermingham, D.H. StJohn, J. Krynen, S. Tedman-Jones, M.S. Dargusch, Promoting the columnar to equiaxed transition and grain refinement of titanium alloys during additive manufacturing, Acta Mater. 168 (2019) 261–274.
[24] T. Zhang, D. Wang, J. Zhu, H. Xiao, C.T. Liu, Y. Wang, Non-conventional transformation pathways and ultrafine lamellar structures in γ-TiAl alloys, Acta Mater. 189 (2020) 25–34.
[25] Q. Wang, K. Zhang, W. Niu, Microstructural characteristic and mechanical properties of titanium-copper alloys in-situ fabricated by selective laser melting, J. Alloys Compd. 885 (2021) 161032.
[26] H. Beladi, Q. Chao, G.S. Rohrer, Variant selection and intervariant crystallographic planes distribution in martensite in a Ti–6Al–4V alloy, Acta Mater. 80 (2014) 478–489.
[27] P.L. Stephenson, N. Haghdadi, R. DeMott, X.Z. Liao, S.P. Ringer, S. Primig, Effect of scanning strategy on variant selection in additively manufactured Ti-6Al-4V, Addit. Manuf. 36 (2020) 101581.
[28] Z. Yao, T. Yang, M. Yang, X. Jia, C. Wang, J. Yu, Z. Li, H. Han, W. Liu, G. Xie, S. Yang, Q. Zhang, C. Wang, S. Wang, X. Liu, Martensite colony engineering: a novel solution to realize the high ductility in full martensitic 3D-printed Ti alloys, Mater. Des. 215 (2022) 110445.
[29] D. Liu, J. Wang, C. Wang, P. Jiang, F. Yuan, X. Wu, Hetero-deformation-induced (HDI) plasticity induces simultaneous increase in both yield strength and ductility in a Fe50Mn30Co10Cr10 high-entropy alloy, Appl. Phys. Lett. 119 (13) (2021).
[30] X. Wu, Y. Zhu, K. Lu, Ductility and strain hardening in gradient and lamellar structured materials, Scripta Mater. 186 (2020) 321–325.
[31] X. Feaugas, On the origin of the tensile flow stress in the stainless steel AISI 316L at 300 K: back stress and effective stress, Acta Mater. 47 (13) (1999) 3617–3632.
[32] X. Wu, M. Yang, F. Yuan, G. Wu, Y. Wei, X. Huang, Y. Zhu, Heterogeneous lamella structure unites ultrafine-grain strength with coarse-grain ductility, Proc. Natl. Acad. Sci. USA 112 (47) (2015) 14501–14505.